scientific reports

Check for updates

OPEN

Mechanisms of temperature effects on the tensile properties and dislocation behavior of Mg-Zn-Ca alloys

Yang Yu[1], Yuhao Wei[2], Yaoyao Song[3], Haoge Shou[4]✉ & Liuyong He[5]

This study investigates the influence mechanisms of temperature on the tensile properties of Mg-Zn-Ca alloys, with a focus on the activation differences of slip systems at room temperature (RT) and high temperature (HT), and their effects on work hardening behavior. Observations using electron backscatter diffraction (EBSD) and transmission electron microscopy (TEM) reveal that Mg-Zn-Ca alloy deformation predominantly relies on basal slip and partial pyramidal slip at RT. The decomposition of pyramidal <c + a> into basal <c + a> dislocations enhance dislocation interactions, which increases the work hardening rate and tensile strength. In contrast, more non-basal and multi-slip systems are activated at HT, reducing dislocation interactions and leading to a decrease in the work hardening rate. The HT samples exhibit lower tensile strength but higher elongation. This study reveals the regulatory mechanism of pyramidal <c + a> dislocation slip decomposition and dislocation interactions at different temperatures, providing a theoretical foundation for designing high-strength, high-ductility magnesium alloys.

Keywords Mg-Zn-Ca alloy, Temperature dependence, Slip system, Dislocation decomposition, Work hardening

Magnesium (Mg) alloys as a lightweight metallic material, are widely used in aerospace, automotive, and electronics industries due to their excellent specific strength, specific stiffness, good corrosion resistance, and recyclability[1–3]. In recent years, research on Mg alloys has primarily focused on improving their mechanical properties. In particular, studies on the high-temperature (HT) mechanical properties of Mg alloys have become an important direction for optimizing material design and enhancing performance[4,5]. The deformation behavior of Mg alloys largely depends on their hexagonal close-packed (HCP) crystal structure and the activation of different slip systems[6,7]. Temperature variations significantly influence the activation of these slip systems and strain distribution, thereby affecting the mechanical properties of Mg alloys[8,9].

At room temperature (RT), Mg alloys primarily deform through basal slip[10,11]. However, due to the limited deformation coordination capacity of basal slip and its strong directional dependence, Mg alloys often exhibit low plasticity at RT[12,13]. To improve the plasticity of Mg alloys, researchers have proposed activating non-basal slip systems by controlling alloy composition, optimizing processing techniques, or introducing heterogeneous structures[10,14–16]. To some extent, the activation of these non-basal slip systems can enhance the plastic deformation ability of Mg alloys[17,18]. Furthermore, temperature as one of the key factors influencing the deformation behavior of Mg alloys, can significantly alter the activation of slip systems and dislocation motion behavior, thereby affecting their mechanical properties[19,20]. At high temperatures, the lattice energy of the alloy increases, and the resistance to dislocation motion decreases, making it easier to activate slip systems other than basal slip[21]. Additionally, dislocation interactions affect the deformation mode and work hardening behavior of the alloy, further influencing its mechanical properties[22].

Deformed Mg alloys exhibit a strong basal texture at RT, resulting in poor formability and severely limiting their applications. Alloying can weaken the basal texture of deformed Mg alloys, thereby improving the formability of Mg alloy sheets. Based on this, researchers have developed Mg-Zn-Ca alloys, where the addition

[1]Center for Engineering and Technology, Huanghuai University, Zhumadian 463000, China. [2]School of Computer Science, University of Sydney, Sydney, NSW, Australia. [3]Logistics Service Center, Huanghuai University, Zhumadian 463000, China. [4]College of Intelligent Manufacturing, Huanghuai University, 76 Kaiyuan Road, Yicheng District, Zhumadian 463000, China. [5]College of Materials Science and Engineering, Chongqing University, Chongqing 400044, China. ✉email: 20212249@huanghuai.edu.cn

of Zn and Ca weakens the strong basal texture of deformed Mg alloys and enhances their formability[23–25]. This is primarily attributed to Ca and Zn promoting the activation of extension twinning and non-basal slip, thereby increasing the diversity of deformation modes and weakening the basal texture[23,24]. Furthermore, the addition of Ca and Zn influences the recrystallization behavior of Mg alloys, promoting the formation of non-equiaxed grains and consequently suppressing the formation of basal texture[26,27]. In recent years, Mg-Zn-Ca alloys have received widespread attention due to their excellent mechanical properties and biocompatibility[28–31]. In addition, the addition of Zn and Ca not only enhances the alloy's strength but also improves its mechanical properties by refining the grain structure, and forming second-phase particles[28,31–33]. Naghdi et al.[34] investigated the shear deformation behavior of extruded Mg-4Zn-0.5Ca alloy at RT using shear punch testing and quantified the contributions of different strengthening mechanisms to the shear yield stress and overall flow stress of the material. The results indicate that grain boundary and solid solution strengthening make significant contributions to the overall strength of the material, whereas the contributions of second-phase particles and dislocations are negligible. Subsequently, Naghdi et al.[35] further investigated the high-temperature shear mechanical properties of as-cast and aged Mg-4Zn-0.5Ca alloys. The results revealed that aging treatment induces the formation of a semi-continuous network structure composed of equiaxed α-Mg grains and coarse $Ca_2Mg_6Zn_3$ phases, along with the precipitation of nanoscale phases in the interior of grains. These phases exhibit high thermal stability and significantly enhance the high-temperature mechanical properties of the aged samples. However, the deformation mechanisms of Mg-Zn-Ca alloys at different temperatures and their effects on mechanical properties have not been fully studied. In particular, how temperature influences the activation of slip systems, dislocation behavior, and work hardening remains a hot topic in current research.

This study aims to explore the temperature-dependent mechanisms affecting the tensile properties of Mg-Zn-Ca alloys, focusing on the differences in slip system activation at different temperatures and their impact on the alloy's mechanical properties. By comparing the deformation behavior of the alloy under both RT and HT conditions, and combining microstructural characterization and mechanical performance testing, this study further reveals the influence of temperature on the alloy's deformation modes, work hardening rate, and tensile properties. In addition, the study will delve into the changes in the activation mechanisms of slip systems caused by temperature, particularly examining the role of cone slip at different temperatures, thus providing a theoretical basis for optimizing the high strength and high ductility of Mg-Zn-Ca alloys.

Materials and methods

Material preparation and characterization

The material used in this study is a Mg-2Zn-0.1Ca alloy, with cast ingots purchased from the Baotou Rare Earth Research Institute. The composition of the alloy was determined using Inductively Coupled Plasma Optical Emission Spectroscopy (ICP-OES), as shown in Table 1. The samples were cut into plates measuring $80 \times 70 \times 5$ mm and subjected to a homogenization treatment at 350 °C for 24 h. Subsequently, the samples were hot-rolled at 350 °C, with a reduction in thickness of 20% per pass, eventually achieving a final thickness of approximately 1 mm. The hot-rolled samples were then annealed at 400 °C for 40 min.

Tensile tests were conducted at RT and 175 °C, with a strain rate of 1×10^{-3} s^{-1}. The samples subjected to RT and 175 °C tensile testing was labeled as RT and HT samples, respectively. The tensile specimens were dog-bone shaped, with gauge dimensions of 70 (Rolling direction, RD) × 4 (Transverse direction, TD) × 1 mm (Normal direction, ND). At least three samples were tested under each condition to ensure reproducibility.

The microstructures of the RT and HT samples were characterized using a field-emission scanning electron microscope (SEM, TESCAN MIRA 3) equipped with a HKL electron backscatter diffraction (EBSD) detector. After grinding, the samples were etched with an appropriate corrosive solution at room temperature for SEM observation. For EBSD analysis, the samples were mechanically polished and electrochemically polished using an AC2 solution at -40 °C and 20 V for 160 s.

Slip trace method

Figure 1 illustrates the steps involved in using the slip trace method to identify the activated slip systems. The process is divided into the following four steps:

(1) Identify the region of interest (ROI), which contains at least 500 grains, and mark it using a Vickers hardness tester. (2) Perform SEM imaging (Fig. 1a) of the ROI in the deformed sample and acquire the corresponding EBSD data for the region. (3) Use Channel 5 software to obtain the Euler angles of the grains (Fig. 1b) and match these grains with those exhibiting slip traces (Fig. 1a). (4) Input the Euler angles into a custom Matlab program to calculate the 12 theoretical slip systems[33,36,37]. These are then compared with the observed slip traces to identify the activated slip systems.

Figure 1 shows a representative example of the slip trace method. Figure 1a and b present the SEM image showing the slip traces and the corresponding EBSD data (Euler angles) of the grains, respectively. Figure 1c displays the 12 theoretical slip systems for the grain, while Fig. 1d shows the identified basal slip system for the grain (specifically $(0001)[\bar{1}2\bar{1}0]$).

Composition	Element (wt%)		
	Zn	Ca	Mg
Mg-2Zn-0.1Ca	1.58	0.087	Balance

Table 1. Chemical compositions of the Mg-Zn-Ca alloy.

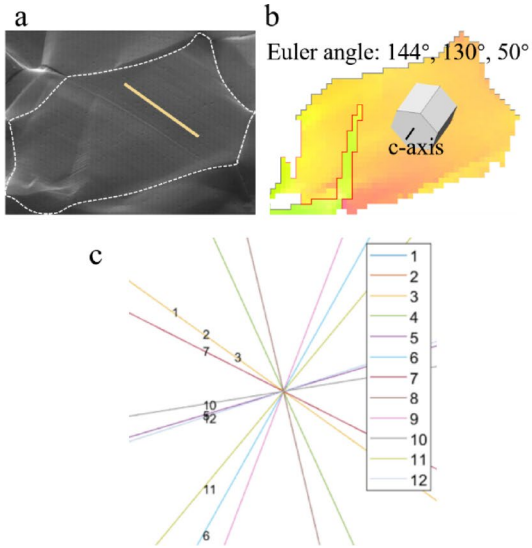

d

Slip system number	Slip system		Schmid factor
1	Basal <a> slip	(0001) [$2\bar{1}\bar{1}0$]	0.2805
2		(0001) [$\bar{1}2\bar{1}0$]	0.3842
3		(0001) [$\bar{1}\bar{1}20$]	0.1037
4	First-order prismatic <a> slip	($0\bar{1}10$) [$2\bar{1}\bar{1}0$]	0.4016
5		($10\bar{1}0$) [$\bar{1}2\bar{1}0$]	0.1993
6		($1\bar{1}00$) [$\bar{1}\bar{1}20$]	0.2023
7	Second-order pyramidal <c+a> slip	($2\bar{1}\bar{1}2$) [$\bar{2}113$]	0.1104
8		($11\bar{2}2$) [$\bar{1}\bar{1}23$]	0.0719
9		($\bar{1}2\bar{1}2$) [$1\bar{2}13$]	0.0370
10		($\bar{2}112$) [$2\bar{1}\bar{1}3$]	0.0161
11		($\bar{1}\bar{1}22$) [$11\bar{2}3$]	0.4212
12		($1\bar{2}12$) [$\bar{1}2\bar{1}3$]	0.2180

Fig. 1. Determination of activated slip systems for specific grains: (**a**) SEM image, (**b**) EBSD data, (**c**) 12 theoretical slip systems, and (**d**) identification of activated slip system.

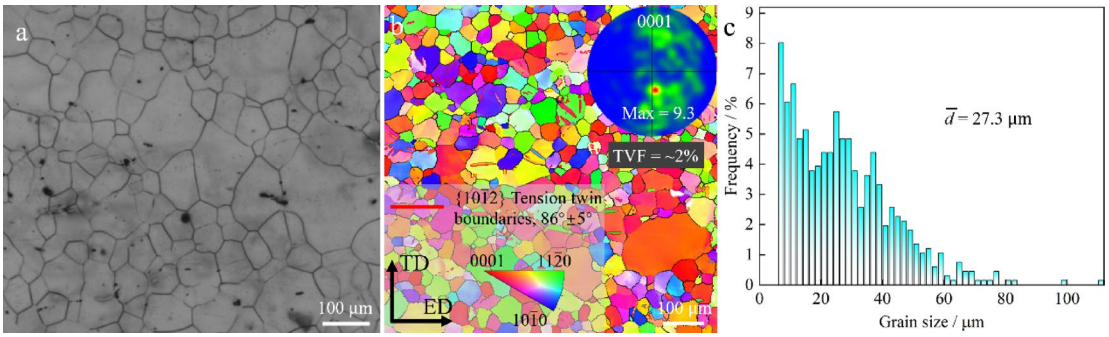

Fig. 2. Initial microstructure of Mg-Zn-Ca sample: (**a**) OM image, (**b**) IPF map, and (**c**) grain size distribution.

Results

Initial microstructure

To elucidate the initial microstructure of the alloy, optical microscopy (OM) characterization of the Mg-Zn-Ca alloy, as shown in Fig. 2a. There no significant phase segregation or formation of substantial secondary phases was observed in the matrix, indicating a weak tendency for phase segregation under the present processing conditions. More key features of the microstructure can be obtained from the inverse pole figure (IPF) and grain size distribution maps presented in Fig. 2b and c. The majority of grains in the Mg-Zn-Ca sample are equiaxed, indicating a relatively uniform grain structure, which is typical of materials processed by methods such as hot rolling or extrusion[38,39]. The extension twin boundary marked by the red solid lines in Fig. 2b, suggest that during the extrusion process, some grains underwent deformation conducive to the activation of the extension twinning. Additionally, the sample exhibits a weak basal texture, with a maximum pole density value of 9.3. Furthermore, EBSD analysis was employed to quantitatively assess the extension twins in the region shown in Fig. 2b, revealing a twin volume fraction (TVF) of approximately 2%. These results further demonstrate that, although a certain amount of extension twins is present, they do not dominate the overall microstructure. Statistical analysis of approximately 500 grains reveals an average grain size of about 27.3 μm, as shown in Fig. 2c. To ensure a statistically representative texture analysis, additional EBSD measurements were performed on the Mg-Zn-Ca samples, covering approximately 1300 grains. The results confirm that the overall texture characteristics are consistent with those presented in Fig. 2. The EBSD map and corresponding texture analysis from this additional measurement are provided in the Supplementary material (Fig. A1).

Mechanical properties

Figure 3 presents the engineering stress-strain and strain hardening curves of the Mg-Zn-Ca samples. Analysis of these curves reveals significant differences in tensile properties and strain hardening behavior between the RT and HT samples. The tensile yield strength (YS) of the RT sample is 103.5 MPa, and the ultimate tensile strength (UTS) is 179.2 MPa, while the YS of the HT sample is 72.6 MPa, and the UTS is 115.9 MPa, as shown in

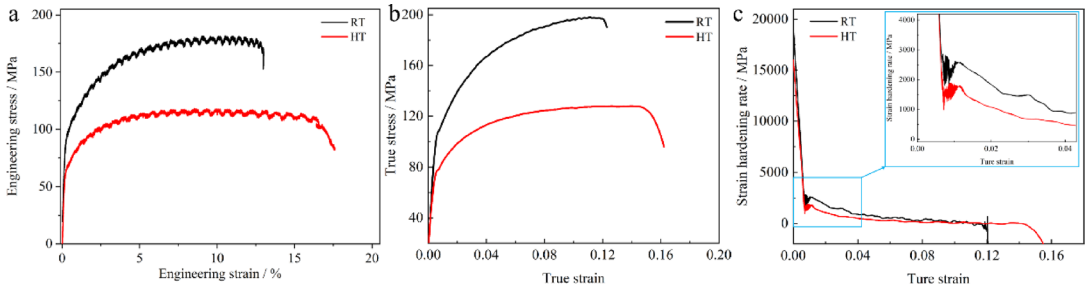

Fig. 3. Mechanical properties of RT and HT samples: (**a**) Engineering stress-strain curve, (**b**) true stress-strain curve, and (**c**) strain hardening curve.

Samples	YS, MPa	UTS, MPa	failure elongation, %
RT	103.5 ± 1.8	179.2 ± 3.2	12.8 ± 2.0
HT	72.6 ± 3.5	115.9 ± 2.0	16.6 ± 3.0

Table 2. Mechanical properties of pure Mg-Zn-Ca samples.

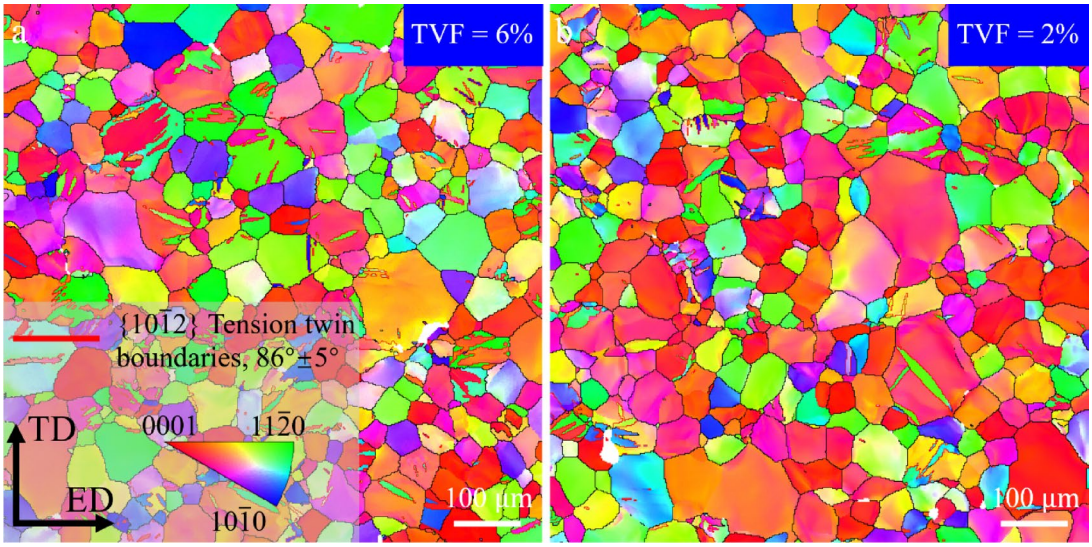

Fig. 4. EBSD data of Mg-Zn-Ca alloy at 5% tensile strain: (**a**) RT sample, and (**b**) HT sample.

Table 2. This indicates that the RT sample exhibits higher strength, allowing it to withstand higher stress before yielding and fracturing. However, the fracture elongation of the HT sample is 16.6%, which is higher than the 12.8% of the RT sample, suggesting that the HT sample possesses better ductility, enabling it to undergo more deformation before failure. The strain hardening curves show that the strain hardening rate of the RT sample is significantly higher than that of the HT sample.

Deformation modes

Figure 4a and b show the IPF maps of the RT and HT samples after 5% tensile strain, with the stretching direction along the RD. It can be observed that the extension TVF in the RT and HT samples is 6% and 2%, respectively. This indicates that dislocation slip is the dominant deformation mode during tensile deformation, rather than twinning.

Figure 5 shows the SEM images of the RT sample after being tensile to 5% strain along the RD. The red lines in Fig. 5 represent basal slip, the blue lines correspond to prismatic slip, and the yellow lines indicate pyramidal slip traces. These traces are distributed across different grains, indicating that the slip activity within each grain was activated during the deformation process. It can be observed that basal slip is the dominant slip mode, covering almost all grains, which is related to its low critical resolved shear stress (CRSS)[40,41]. Additionally, some prismatic and pyramidal slip traces are observed, though they are more limited in distribution, suggesting that the activation of prismatic and pyramidal slip systems is restricted under RT conditions. Furthermore, the slip

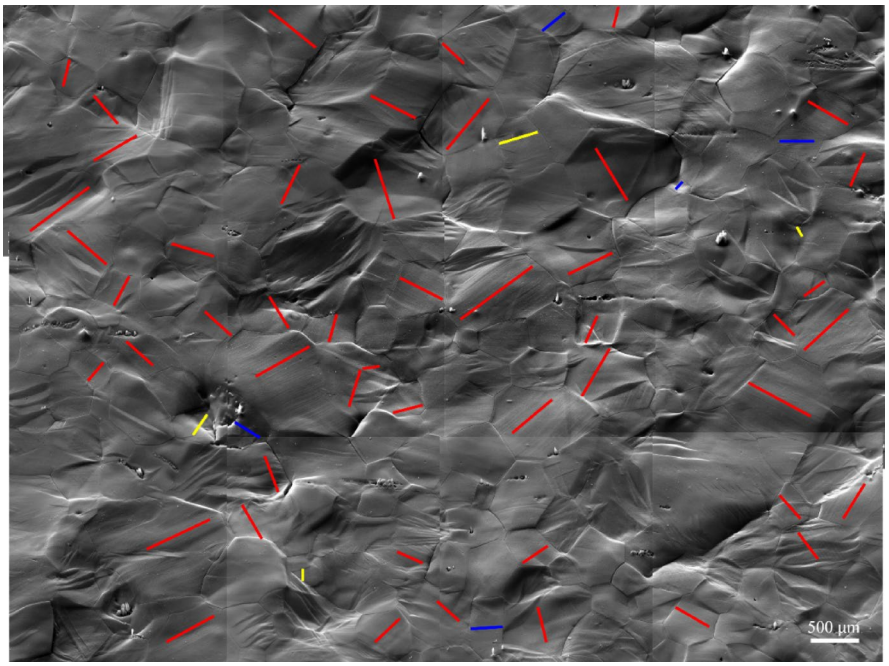

Fig. 5. SEM images of the RT sample at 5% tensile strain.

activity in the RT sample is mainly concentrated in a single slip system. Figure 6a shows the SEM images of the HT sample after being stretched to 5% strain along the RD. Similar to the RT sample, the slip traces are marked with red, blue, and yellow lines representing basal, prismatic, and pyramidal slip systems. However, unlike the RT sample, the HT sample shows an increased number of non-basal slip traces and exhibits a multiple slip phenomenon (within the white dashed box). Figure 6b clearly displays a grain containing two types of slip traces: basal slip and prismatic slip, indicating that under HT conditions, more non-basal slip systems are activated. This may be due to the enhanced ability of dislocation climb and cross-slip at elevated temperatures[42–44].

We also conducted a statistical analysis of the activated slip systems for both the RT and HT samples, as shown in Fig. 7. Basal slip remains the primary deformation mode for both samples. However, compared to the RT sample (15.4%), the HT sample activated more non-basal slip (32.4%). Overall, the two sets of samples exhibit distinctly different slip behaviors at different temperatures. The RT sample predominantly exhibits basal slip, while the HT sample activates more non-basal slip and shows significant multiple slip characteristics. This difference highlights the significant impact of temperature on the slip behavior and tensile properties of Mg alloys, with the enhanced non-basal slip and multiple slip ability at HTs playing a crucial role in improving the material's ductility.

Figure 8 shows the Kernel Average Misorientation (KAM) maps of the RT and HT samples at 5% tensile strain. The KAM value is an important indicator used to measure the lattice misorientation within local grains of the material and is typically employed to describe the distribution of local plastic strain during deformation[45,46]. A higher KAM value indicates greater plastic strain in a local region, usually associated with dislocation density and deformation gradients[47]. Conversely, a lower KAM value suggests smaller plastic deformation in that region. By comparing the KAM maps of the RT sample (Fig. 8a) and HT sample (Fig. 8b), significant differences in strain distribution can be observed. In the KAM map of the RT sample, higher KAM values are mainly distributed near the grain boundaries, indicating the formation of higher strain gradients in local regions, particularly in areas with high dislocation density[47]. The deformation is primarily concentrated on a few slip systems, resulting in a more localized strain distribution and higher average KAM values. In contrast to the RT sample, the KAM distribution map of the HT sample (Fig. 8b and c) exhibits lower average KAM values, with a more uniform strain distribution both within the grains and at the grain boundaries. The average KAM value for the RT sample is 0.95°, while for the HT sample is 0.87°, as shown in Fig. 8c. This phenomenon can be attributed to the change in the deformation mechanism at HT, which activates more non-basal slip systems. The activation of these non-basal slip systems expands the deformation slip channels, reducing dislocation concentration in local regions and leading to a more uniform strain distribution. As a result, the HT sample exhibits lower average KAM values and more uniform strain distribution, which is also a reason for the higher elongation of the HT sample.

Discussion

For Mg alloys, the Schmid Factor (SF) value plays a crucial role in determining the activation of different slip systems. Figure 9 shows the SF maps and SF value distributions for different slip systems in Mg-Zn-Ca alloys. It can be observed that the average SF value of the basal slip system is lower than that of the non-basal slip systems, while the prismatic and pyramidal slip systems have similar average SF values. However, due to the significantly lower CRSS of the basal slip system compared to the non-basal slip systems[17,48], basal slip

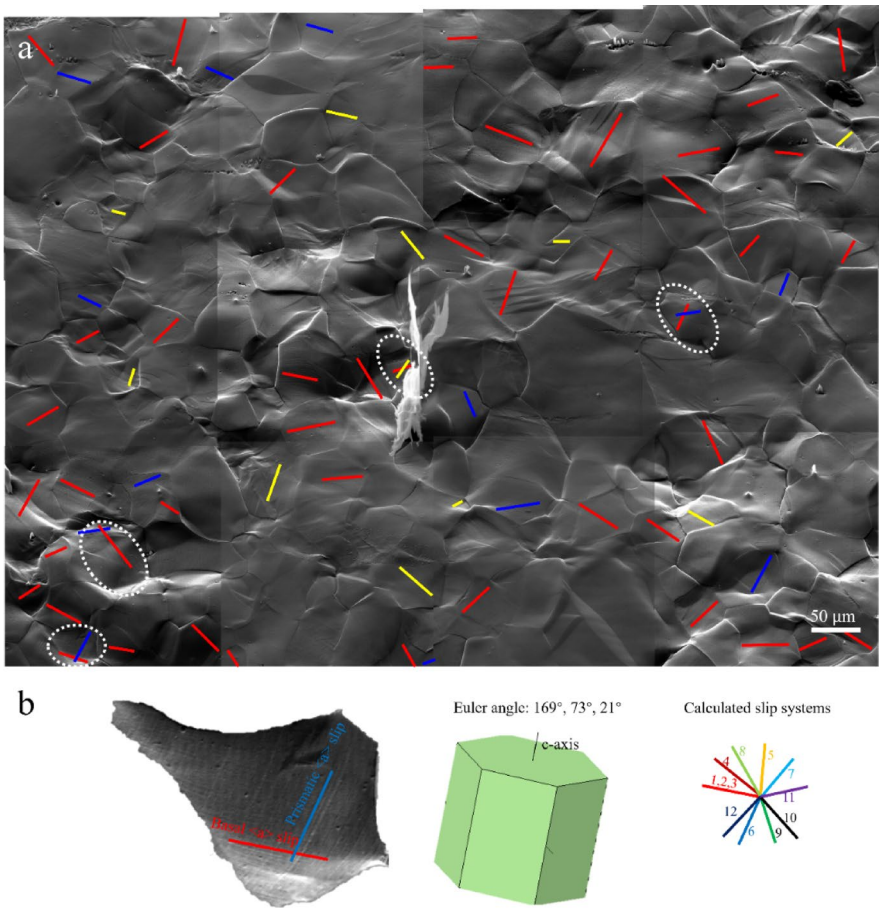

Fig. 6. (**a**) SEM image of the HT sample at 5% tensile strain, and (**b**) grain with cross-slip.

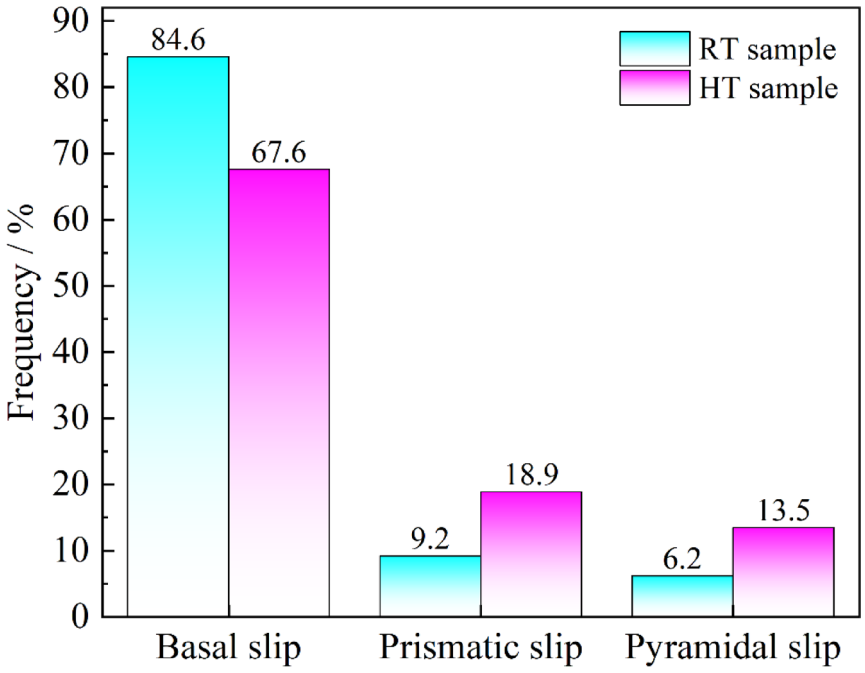

Fig. 7. Statistical chart of activated slip systems in RT and HT samples.

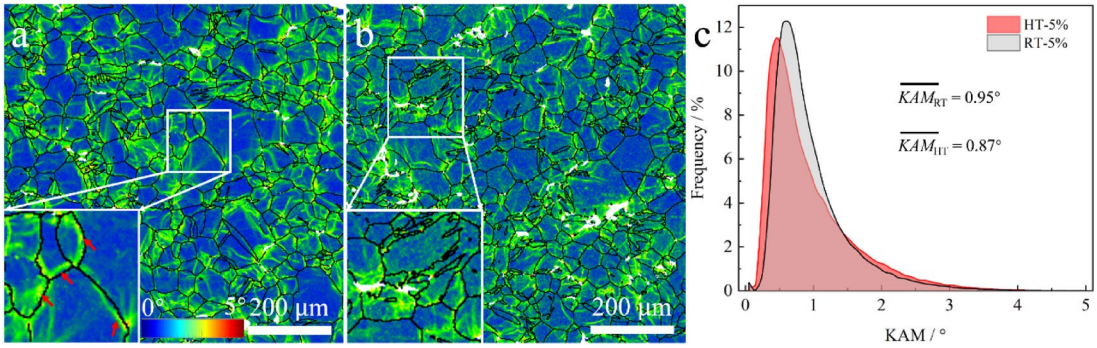

Fig. 8. KAM distribution maps of Mg-Zn-Ca alloy: (**a**) RT sample, (**b**) HT sample, and (**c**) KAM value distribution map.

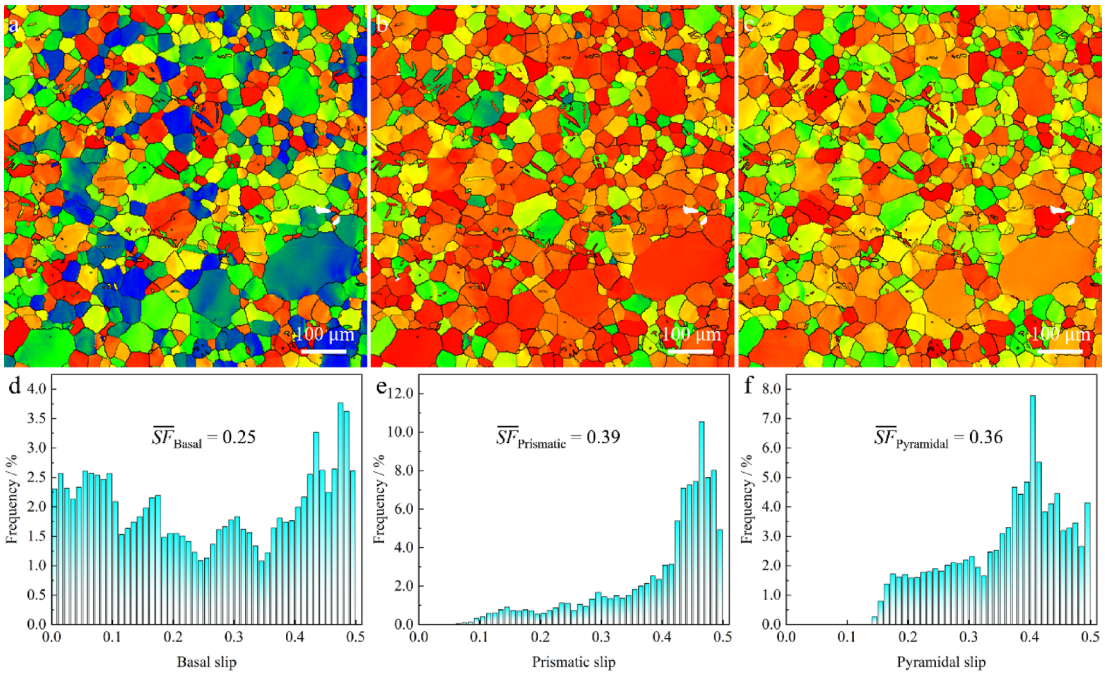

Fig. 9. SF distribution maps of different slip systems in Mg-Zn-Ca alloy: (**a**) and (**d**) basal slip, (**b**) and (**e**) prismatic slip, and (**c**) and (**f**) pyramidal slip.

remains the dominant deformation mode in both RT and HT samples. As the temperature increases, the CRSS of non-basal slip systems decreases, which effectively promotes the activation of non-basal slip systems[21,49,50]. The deformation modes in Mg alloys essentially depend on the relative magnitudes of the CRSS for different slip systems. At room temperature, basal slip becomes the dominant deformation mechanism due to its lowest CRSS (typically around 0.5-1 MPa), while the CRSS of non-basal slip systems, such as prismatic slip and pyramidal < c + a > slip, is as high as 10–50 MPa, resulting in a very low activation probability[40,49,51]. However, an increase in temperature significantly alters this energy barrier distribution: the CRSS of non-basal slip systems is much more temperature-sensitive than that of the basal slip system. As temperature increases, the ratio of CRSS of pyramidal < c + a > slip to CRSS of basal < a > slip decreases, promoting the activation of < c + a > dislocations[52]. Additionally, Zn/Ca alloying suppresses basal slip through solute pinning effects, while lowering the stacking fault energy and promoting dislocation cross-slip[53].

Figure 10 shows the TEM images of RT and HT samples under 5% tensile strain. By analyzing the activation mechanisms of different slip systems during deformation, we aim to explain the differences in work hardening rates between the two samples. It should be noted that all TEM images were taken under the $\boldsymbol{g}=0002$ diffraction condition. According to the extinction condition $\boldsymbol{g}\cdot\boldsymbol{b}=0$[54], < c + a > dislocations can be observed under $\boldsymbol{g}=0002$[14]. From the Fig. 10a and b, it can be seen that a significant number of < c + a > dislocations are present in the RT sample. This can be attributed to the fact that, relying solely on basal slip is insufficient to accommodate the multi-axial strain conditions as strain increases, necessitating additional shear deformation channels provided by pyramidal slip. This is consistent with the results shown in Fig. 7. Furthermore, some

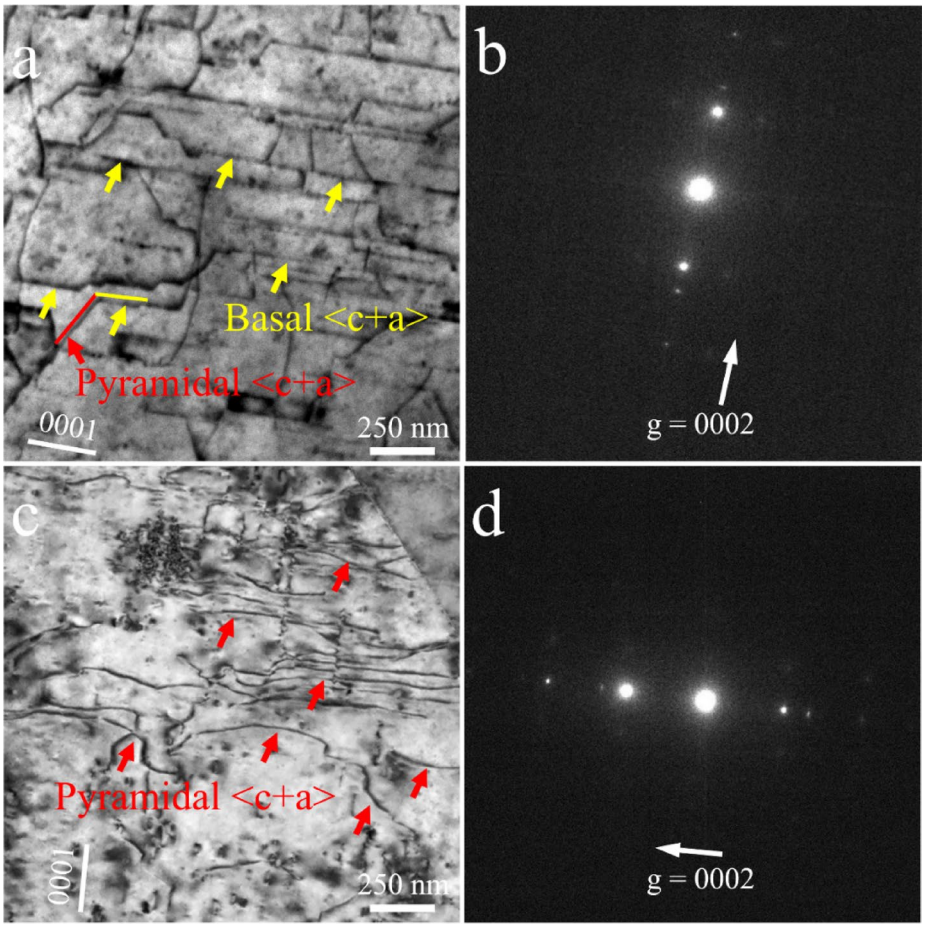

Fig. 10. TEM images and corresponding selected diffraction patterns: (**a**) and (**b**) RT sample, and (**c**) and (**d**) HT sample.

pyramidal < c + a > dislocations may have decomposed towards the basal plane (as indicated by the yellow and red solid lines in Fig. 10a)[13,55]. As reported by Wu et al.[56] and Li et al.[53], <c + a> dislocations distributed on different slip systems exhibit characteristics during deformation that are distinct from those of <a> dislocations. Figure 11a shows the projection of pyramidal II <c + a> dislocations on the $(2\bar{1}\bar{1}0)$ plane. It can be seen that the angle between the pyramidal II plane and the (0001) plane is approximately 62° or 90°. During dislocation glide, various mechanisms, such as cross-slip, dislocation annihilation, and dislocation multiplication collectively influence the evolution of dislocation structures. Figure 11b and c reveal that <c + a> dislocations cross-slip from the pyramidal II plane to the basal plane, indicating that during <c + a> dislocation glide, some dislocation segments transform into basal ⟨c + a⟩ dislocations. These transformed dislocation segments form a stepped dislocation arrangement during subsequent slips. These observations are consistent with the results reported by Li et al.[53]. Notably, the basal <c + a> dislocation segments are sessile and can hinder further dislocation glide. This decomposition mechanism not only enhances dislocation interactions but also increases dislocation entanglement and pile-up, significantly improving the material's work hardening rate[56]. As a result, the RT sample exhibits a higher work hardening rate, which is consistent with its higher tensile strength. In contrast, as shown in Fig. 10c and d, a significant number of pyramidal < c + a > dislocations are also observed in the HT sample, with a more uniform distribution of dislocations. At HT, due to thermal activation, non-basal slip is more easily activated, reducing the deformation limitations of a single slip system. Moreover, the reduced resistance to dislocation motion at HTs weakens the interactions between slip systems, which in turn reduces dislocation entanglement[55]. This results in a lower work hardening rate for the HT sample, which is characterized by lower tensile strength but higher elongation.

It is worth noting that the decomposition tendency of pyramidal < c + a > dislocations have a significant impact on the work hardening rate. If pyramidal slip in the HT sample does not tend to decompose towards the basal plane, the interactions between dislocations will be significantly reduced, leading to an increased average free slip distance for dislocations and further decreasing the work hardening rate. In contrast, in the RT sample, some pyramidal slip dislocations decompose towards the basal plane, which not only provides more dislocation interaction areas but also enhances the dislocation entanglement effect, thereby significantly increasing the work hardening rate. The above analysis explains the differences in work hardening rates between the two samples and

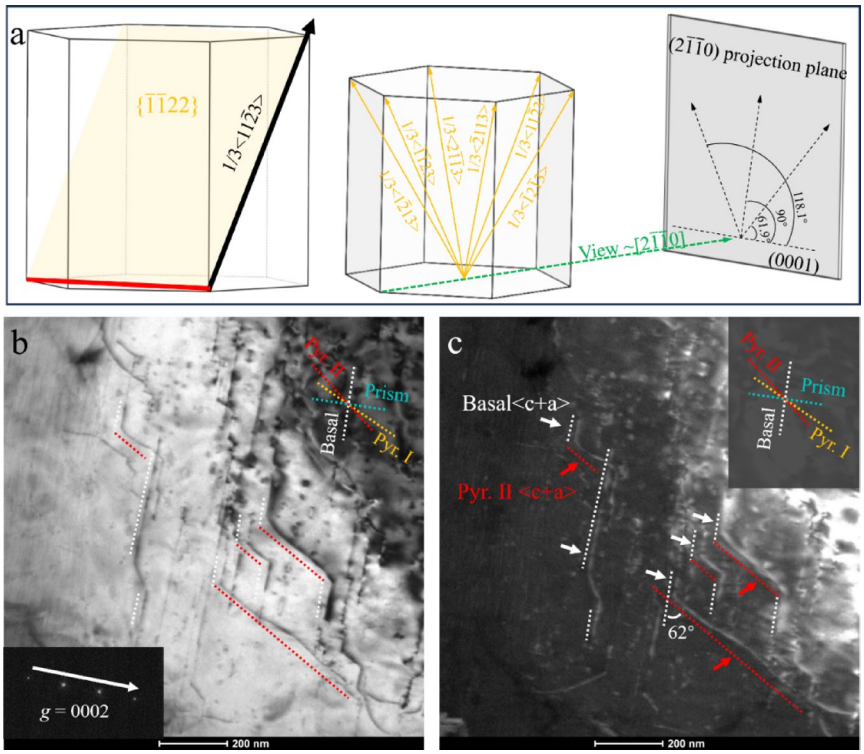

Fig. 11. Typical dislocation configuration in the HT samples: (**a**) a schematic of slip plan and direction for pyramidal II < c + a > dislocations, and projections of < 11$\bar{2}$3> direction along [2$\bar{1}\bar{1}$0], (**b**) and (**c**) TEM images viewed at $g = 0002$.

further reveals the profound impact of temperature on the slip mechanism and deformation behavior of Mg-Zn-Ca alloys. This mechanism analysis is crucial for optimizing the mechanical properties of Mg alloys.

Moreover, it should be noted that in Mg alloys, grain size also has a significant impact on the activation of slip systems. Wei et al.[57] prepared fine-grained pure Mg samples (grain size of 5.5 μm) using high-pressure torsion (HPT) and observed a substantial amount of <c + a> dislocation slip during deformation. They concluded that grain refinement promotes the activation of <c + a> dislocations, which is a key reason for the material's high strength and ductility. Luo et al.[51] used accumulative roll-bonding (ARB) to fabricate fine-grained Mg-3Gd samples (grain size of 3.3 μm) and found a high proportion of pyramidal <c + a> dislocation slip in the deformed samples. Similarly, Koike et al.[58] processed fine-grained AZ31 alloy samples (grain size of 6.5 μm) using equal channel angular pressing (ECAP) and observed a significant amount of <c + a> dislocation slip during plastic deformation. They attributed the excellent ductility (elongation of 47%) to this slip behavior. However, in this study, it was found that the grain sizes of the RT and HT samples did not show a significant difference. Therefore, temperature is considered the primary factor influencing mechanical properties and dislocation slip.

Conclusions

In this study, the effects of temperature on the mechanical properties, deformation modes, and dislocation behavior of Mg-Zn-Ca alloy samples were investigated through tensile deformation at both room temperature and high temperature. The main conclusions are as follows:

1. At room temperature, Mg-Zn-Ca alloy primarily undergoes basal slip, with localized strain concentration. At high temperature, non-basal slip systems are significantly activated, leading to a more uniform strain distribution and improved ductility.
2. At room temperature, pyramidal < c + a > dislocations tend to decompose towards the basal plane, enhancing dislocation interactions and resulting in higher work hardening rates. In contrast, at high temperature, dislocation decomposition decreases, dislocation motion resistance is reduced, and the work hardening rate significantly decreases.
3. Under high-temperature conditions, the activation of non-basal slip systems and the occurrence of multi-slip significantly increase, expanding the deformation channels and reducing local strain concentration, thereby improving the material's ductility.
4. Compared with other Mg alloys, the Mg-Zn-Ca alloy studied in this work exhibits a remarkable ability to activate non-basal slip at elevated temperatures, which is beneficial for enhancing ductility while maintaining reasonable strength. This suggests that optimizing the deformation temperature is an effective strategy for improving the mechanical properties of Mg-Zn-Ca alloys, making them more suitable for structural applications requiring both high strength and ductility.

Data availability

The datasets used and/or analysed during the current study available from the corresponding author on reasonable request.

Received: 14 February 2025; Accepted: 8 May 2025
Published online: 24 May 2025

References

1. Olalekan, O. N., Hassan, S. F., Al-Ahmed, A., Mahar, N. & Nouari, S. Nb2CTx MXene reinforcement stimulated microstructure and mechanical properties of magnesium. *Sci. Rep.* **13** https://doi.org/10.1038/s41598-023-41067-8 (2023).
2. Shahabi-Navid, M. et al. On the early stages of localised atmospheric corrosion of magnesium-aluminium alloys. *Sci. Rep.* **10** https://doi.org/10.1038/s41598-020-78030-w (2020).
3. Li, J. L., Wu, D., Chen, R. S. & Han, E. H. Anomalous effects of strain rate on the room-temperature ductility of a cast Mg-Gd-Y-Zr alloy. *Acta Mater.* **159**, 31–45. https://doi.org/10.1016/j.actamat.2018.08.013 (2018).
4. Srinivasan, A., Pillai, U. T. S., Swaminathan, J. & Pai, B. C. Enhanced high temperature properties of low pressure cast AZ91 Mg alloy. *Int. J. Cast. Met. Res.* **19**, 265–268. https://doi.org/10.1179/136404606x147774 (2006).
5. Serak, J., Simon, C. & Vojtech, D. Properties of MgCaZr alloys. *Manuf. Technol.* **22**, 461–470. https://doi.org/10.21062/mft.2022.054 (2022).
6. Somekawa, H., Singh, A., Sahara, R. & Inoue, T. Excellent room temperature deformability in high strain rate regimes of magnesium alloy. *Sci. Rep.* **8** https://doi.org/10.1038/s41598-017-19124-w (2018).
7. Cepeda-Jiménez, C. M., Molina-Aldareguia, J. M. & Pérez-Prado, M. T. Effect of grain size on slip activity in pure magnesium polycrystals. *Acta Mater.* **84**, 443–456. https://doi.org/10.1016/j.actamat.2014.10.001 (2015).
8. Liang, W., Guan, L., Lv, Q. & Xing, Z. Research on multipass hot spinning process technology of AZ80 magnesium alloy shell. *Adv. Mater. Sci. Eng.* **2019** https://doi.org/10.1155/2019/8930134 (2019).
9. Guo, L. & Fujita, F. Effect of deformation mode, dynamic recrystallization and twinning on rolling texture evolution of AZ31 magnesium alloys. *Trans. Nonferrous Met. Soc. China*. **28**, 1094–1102. https://doi.org/10.1016/s1003-6326(18)64745-4 (2018).
10. Liu, Y. et al. On the heterogeneous microstructure and strengthening mechanisms in a laser welding AZ80 magnesium alloy. *Sci. Rep.* **14** https://doi.org/10.1038/s41598-024-73767-0 (2024).
11. Wei, K. et al. Grain size effect on tensile properties and slip systems of pure magnesium. *Acta Mater.* **206** https://doi.org/10.1016/j.actamat.2020.116604 (2021).
12. Zhu, G. et al. Improving ductility of a Mg alloy via non-basal < a > slip induced by Ca addition. *Int. J. Plast.* **120**, 164–179. https://doi.org/10.1016/j.ijplas.2019.04.020 (2019).
13. Wu, Z. & Curtin, W. A. The origins of high hardening and low ductility in magnesium. *Nature* **526**, 62–67. https://doi.org/10.1038/nature15364 (2015).
14. Pan, H. et al. Mechanistic investigation of a low-alloy Mg–Ca-based extrusion alloy with high strength–ductility synergy. *Acta Mater.* **186**, 278–290. https://doi.org/10.1016/j.actamat.2020.01.017 (2020).
15. Stanford, N. & Barnett, M. R. The origin of rare earth texture development in extruded Mg-based alloys and its effect on tensile ductility. *Mater. Sci. Eng. A*. **496**, 399–408. https://doi.org/10.1016/j.msea.2008.05.045 (2008).
16. Liu, S. et al. Effect of texture on deformation behavior of heterogeneous Mg-13Gd alloy with strength–ductility synergy. *J. Mater. Sci. Technol.* **113**, 271–286. https://doi.org/10.1016/j.jmst.2021.09.065 (2022).
17. Zhao, D. et al. Significant disparity of non-basal dislocation activities in hot-rolled highly-textured Mg and Mg-3Al-1Zn alloy under tension. *Acta Mater.* **207** https://doi.org/10.1016/j.actamat.2021.116691 (2021).
18. Xia, N. et al. Enhanced ductility of Mg–1Zn–0.2Zr alloy with dilute Ca addition achieved by activation of non-basal slip and twinning. *Mater. Sci. Eng. A*. **813** https://doi.org/10.1016/j.msea.2021.141128 (2021).
19. Li, J. et al. The role of dislocation-solute interactions on the creep behaviour of binary Mg-RE alloys. *Sci. Rep.* **11** https://doi.org/10.1038/s41598-021-82517-5 (2021).
20. Ghorbanpour, S., McWilliams, B. A. & Knezevic, M. Effects of environmental temperature and sample pre-straining on high cycle fatigue strength of WE43-T5 magnesium alloy. *Int. J. Fatigue*. **141** https://doi.org/10.1016/j.ijfatigue.2020.105903 (2020).
21. Feng, Y. et al. In-situ synthesizing Al-Y precipitates in Mg-3Y/Al composites for enhancing high-temperature tensile properties. *J. Mater. Res. Technol.* **32**, 3025–3037. https://doi.org/10.1016/j.jmrt.2024.08.113 (2024).
22. Feng, Y., Luan, S., Liu, Q., Liu, Y. & Wang, J. Microstructures evolution and mechanical properties of dilute Mg-Y-Al-Ca-Mn alloy during uniaxial compression deformation at different strain levels. *Mater. Today Commun.* **38** https://doi.org/10.1016/j.mtcomm.2024.108455 (2024).
23. Nakano, H. et al. {10–12} twins in the rolled Mg-Zn-Ca alloy with high formability. *J. Mater. Res.* **39**, 19–22. https://doi.org/10.1557/jmr.2014.358 (2014).
24. Yan, H. Activation of {10–12} twinning and slip in high ductile Mg-2.0Zn-0.8Gd rolled sheet with non-basal texture during tensile deformation at room temperature. *J. Alloys Compd.* **566**, 98–107. https://doi.org/10.1016/j.jallcom.2013.03.008 (2013).
25. Zhao, L. Q. et al. Development of weak-textured and high-performance Mg–Zn–Ca alloy sheets based on Zn content optimization. *J. Alloys Compd.* **849**, 156640. https://doi.org/10.1016/j.jallcom.2020.156640 (2020).
26. Song, J. Zn addition on hot tearing behaviour of Mg-0.5Ca-xZn. *Mater. Des.* **87**, 157–170. https://doi.org/10.1016/j.matdes.2015.08.026 (2015).
27. Homma, T. Effect of Zr addition on the mechanical properties of as-extruded Mg-Zn-Ca-Zr alloy. *Mater. Sci. Eng. A*. **527**, 2356–2362. https://doi.org/10.1016/j.msea.2009.12.024 (2009).
28. Shou, H. et al. Quasi-in-situ analysis of dependency of deformation mechanism and work-hardening behavior on texture in Mg-2Zn-0.1Ca alloy. *J. Alloys Compd.* **784**, 1187–1197. https://doi.org/10.1016/j.jallcom.2019.01.159 (2019).
29. Wang, J. et al. Origins of high ductility exhibited by an extruded magnesium alloy Mg-1.8Zn-0.2Ca: experiments and crystal plasticity modeling. *J. Mater. Sci. Technol.* **84**, 27–42. https://doi.org/10.1016/j.jmst.2020.12.047 (2021).
30. Wang, J., Chen, Y., Chen, Z., Llorca, J. & Zeng, X. Deformation mechanisms of Mg-Ca-Zn alloys studied by means of micropillar compression tests. *Acta Mater.* **217** https://doi.org/10.1016/j.actamat.2021.117151 (2021).
31. Huang, X. et al. Understanding the mechanisms of texture evolution in an Mg-2Zn-1Ca alloy during cold rolling and annealing. *Int. J. Plast.* **158** https://doi.org/10.1016/j.ijplas.2022.103412 (2022).
32. Prasad, S. V. S. et al. The role and significance of magnesium in modern day research-A review. *J. Magnes Alloy*. **10**, 1–61. https://doi.org/10.1016/j.jma.2021.05.012 (2022).
33. He, L. et al. The effect of precipitates on low-cycle fatigue behavior of WE54 magnesium alloys under stress-controlled mode. *Int. J. Fatigue*. **179** https://doi.org/10.1016/j.ijfatigue.2023.108061 (2024).
34. Naghdi, F. et al. Contributions of different strengthening mechanisms to the shear strength of an extruded Mg–4Zn–0.5Ca alloy. *Philos. Mag.* **95**, 3452–3466. https://doi.org/10.1080/14786435.2015.1083134 (2015).
35. Naghdi, F. et al. Microstructure and high-temperature mechanical properties of the Mg–4Zn–0.5Ca alloy in the as-cast and aged conditions. *Mater. Sci. Eng. A*. **649**, 441–448. https://doi.org/10.1016/j.msea.2015.10.011 (2015).

36. He, L. et al. Towards extraordinary strength-ductility synergy in pure Mg via dislocation transmutation. *Int. J. Plast.* **183** https://doi.org/10.1016/j.ijplas.2024.104160 (2024).
37. Li, T. et al. Towards strength-ductility synergy in a weak-textured Mg-3Y extruded sheet via pre-twinning and annealing. *Mater. Sci. Eng. A*. **888** https://doi.org/10.1016/j.msea.2023.145812 (2023).
38. Tripathy, S. & Ghosh Chowdhury, S. On the through-process texture evolution assessment in grain oriented Fe-3 Wt% Si steel produced by a novel directional inoculation technique. *Sci. Rep.* **11** https://doi.org/10.1038/s41598-021-84360-0 (2021).
39. Yin, S. et al. Achieving excellent superplasticity of Mg-7Zn-5Gd-0.6Zr alloy at low temperature regime. *Sci. Rep.* **9** https://doi.org/10.1038/s41598-018-38420-7 (2019).
40. Cepeda-Jimenez, C. M., Castillo-Rodriguez, M. & Perez-Prado, M. T. Origin of the low precipitation hardening in magnesium alloys. *Acta Mater.* **165**, 164–176. https://doi.org/10.1016/j.actamat.2018.11.044 (2019).
41. Liu, Y. et al. Grain refinement mechanism in gradient nanostructured Mg-Gd-Y-Zn-Zr alloy prepared by severe shear deformation. *Mater. Sci. Eng. A*. **894** https://doi.org/10.1016/j.msea.2024.146207 (2024).
42. Suzuki, M., Sato, H., Maruyama, K. & Oikawa, H. Creep deformation behavior and dislocation substructures of Mg-Y binary alloys. *Mater. Sci. Eng. A*. **319**, 751–755. https://doi.org/10.1016/s0921-5093(01)01005-x (2001).
43. Trojanová, Z. & Lukác, P. Compressive deformation behaviour of magnesium alloys. *J. Mater. Process. Technol.* **162**, 416–421. https://doi.org/10.1016/j.jmatprotec.2005.02.024 (2005).
44. Zhang, Y. et al. Effects of initial texture on the three-dimensional creep anisotropic behaviors of dilute Mg-Y binary alloy sheets. *Mater. Sci. Eng. A*. **766** https://doi.org/10.1016/j.msea.2019.138336 (2019).
45. Li, T. et al. Anisotropic cyclic deformation behavior of an extruded Mg-3Y alloy sheet with rare Earth texture. *J. Magnes Alloy*. **10**, 1581–1597. https://doi.org/10.1016/j.jma.2022.05.010 (2022).
46. Hielscher, R., Silbermann, C. B., Schmidl, E. & Ihlemann, J. Denoising of crystal orientation maps. *J. Appl. Crystallogr.* **52**, 984–996. https://doi.org/10.1107/s1600576719009075 (2019).
47. Li, T. et al. Tailoring texture to highly strengthen AZ31 alloy plate in the thickness direction via pre-tension and rolling-annealing. *Acta Metall. Sin -Engl Lett.* **36**, 266–280. https://doi.org/10.1007/s40195-022-01460-0 (2023).
48. Victoria-Hernández, J., Yi, S. & Letzig, D. Role of non-basal slip systems on the microstructure and texture development of ZXK-Mg alloy deformed in plane strain compression at elevated temperature. *Scr. Mater.* **208** https://doi.org/10.1016/j.scriptamat.2021.114322 (2022).
49. Chapuis, A. & Liu, Q. Investigating the temperature dependency of plastic deformation in a Mg-3Al-1Zn alloy. *Mater. Sci. Eng. A*. **725**, 108–118. https://doi.org/10.1016/j.msea.2018.04.019 (2018).
50. Fan, H., Wang, Q., Tian, X. & El-Awady, J. A. Temperature effects on the mobility of pyramidal dislocations in magnesium. *Scr. Mater.* **127**, 68–71 https://doi.org/10.1016/j.scriptamat.2016.09.002 (2017).
51. Luo, X. et al. Transitions in mechanical behavior and in deformation mechanisms enhance the strength and ductility of Mg-3Gd. *Acta Mater.* **183**, 398–407. https://doi.org/10.1016/j.actamat.2019.11.034 (2020).
52. Feng, Y. et al. Achievement of excellent high-temperature mechanical properties of AZ31/ Mg3Y laminated composite by in situ synthesis of Al-Y precipitates. *Mater. Sci. Eng. A*. **921**, 147573. https://doi.org/10.1016/j.msea.2024.147573 (2024).
53. Li, M. et al. Mechanism of strain hardening of magnesium single-crystals: discrete dislocation dynamics simulations. *J. Mech. Phys. Solids*. **173**, 105238. https://doi.org/10.1016/j.jmps.2023.105238 (2023).
54. He, L. et al. Towards extraordinary strength-ductility synergy in pure Mg via dislocation transmutation. *Int. J. Plast.* https://doi.org/10.1016/j.ijplas.2024.104160 (2024).
55. Li, M., Tian, X., Jiang, W., Wang, Q. & Fan, H. Mechanism of strain hardening of magnesium single-crystals: discrete dislocation dynamics simulations. *J. Mech. Phys. Solids*. **173** https://doi.org/10.1016/j.jmps.2023.105238 (2023).
56. Wu, Z. & Curtin, W. A. The origins of high hardening and low ductility in magnesium. *Nature* **526**, 62–. https://doi.org/10.1038/nature15364 (2015).
57. Wei, K. et al. Grain size effect on tensile properties and slip systems of pure magnesium. *Acta Mater.* **206**, 116604. https://doi.org/10.1016/j.actamat.2020.116604 (2021).
58. Koike, J. et al. The activity of non-basal slip systems and dynamic recovery at room temperature in fine-grained AZ31B magnesium alloys. *Acta Mater.* **51**, 2005–2065. https://doi.org/10.1016/s1359-6454(03)00005-3 (2003).

Acknowledgements

This work was supported by foundation of Key Scientific Research Projects of Colleges and Universities in Henan Province, China (No. 23A430040), foundation of Key research and development program of Henan Province, China (No. 241111111600), foundation of Key R and D and Promotion Projects of Henan Province, China (No. 242102230130), foundation of youth Science and Technology Innovation of Zhumadian City, China (No. QNZX202321, QNZX202317), as well as the Cultivation project of National Natural Science Foundation of China of Huanghuai University in 2023.

Author contributions

Yang Yu: Writing - original draft, Writing - review & editing, Conceptualization, Resources, Supervision, Project administration, Funding acquisition. Yuhao Wei: Investigation, Writing - review & editing. YaoYao Song: Writing - review & editing. Haoge Shou: Supervision Project administration, Funding acquisition. Liuyong He: Methodology, Investigation, Writing - review & editing.

Declarations

Competing interests

The authors declare no competing interests.

Additional information

Supplementary Information The online version contains supplementary material available at https://doi.org/10.1038/s41598-025-01805-6.

Correspondence and requests for materials should be addressed to H.S.